

In-situ micro-rheology of a foulant layer at a membrane surface

José A. Epstein^a, Guy Z. Ramon^{b,*}

^a Department of Civil & Environmental Engineering, Technion – Israel Institute of Technology, Haifa 32000, Israel

^b Department of Civil & Environmental Engineering and Department of Chemical Engineering, Technion – Israel Institute of Technology, Haifa 32000, Israel

ARTICLE INFO

Keywords:

Membrane fouling
In-situ analysis
Micro-scale rheology
Extracellular polymeric substances
Foulant depth variations

ABSTRACT

Fouling remains an operational limitation in membrane-based water purification. Despite extensive research on fouling, little is known about the mechanical properties of foulant deposits, their response to operating conditions and how these relate to fouling reversibility and resistance to permeation.

Here, we demonstrate in-situ measurements of the micro-scale rheology of a foulant layer deposited at a membrane surface. A custom-made membrane cell was employed, fabricated with an optical window to enable high-resolution, real-time observation with a confocal microscope. Permeate flux and applied pressure were accurately maintained using a software-based controller. A particle-tracking technique was employed to assess the mechanical properties at different depths within the foulant layer. Through the analysis of particle trajectory statistics, the mechanical properties of the alginate layer are obtained in terms of the frequency-dependent storage and loss modulus.

Importantly, this method enables the simultaneous measurement of foulant layer micro-mechanics and its macroscopic manifestation — the hydraulic resistance during filtration. Results demonstrate the elastic-gel characteristics of the foulant layer, and the variations in its storage and loss moduli upon flux increase, indicating micro-scale ‘stiffening’ of the material, as it undergoes compaction. In addition, the observed increase in the complex viscosity coincides with an increase in the hydraulic resistance. The foulant properties also exhibit clear depth variations, where the foulant’s apparent ‘stiffness’, as manifested by its complex viscosity, increases at closer proximity to the membrane surface. The presented approach provides fundamental insight and opens new possibilities for studying foulant mechanical properties, in-situ, which can lead to more effective cleaning and back-pulsing strategies for foulant removal, e.g., by selecting the most appropriate frequency and intensity.

1. Introduction

While membrane-based separations have become increasingly widespread, fouling is still regarded as one of the main operational limitations in the deployment of membrane-based water purification and desalination [1–4]. In particular, accumulation and attachment of material to the membrane surface results in an increase of the pressure required to maintain the permeate flux, increasing energy consumption and hence, operational costs.

The pressure–flux variations due to fouling have been widely studied [5–8], with particular attention to the relations between the pressure-driven permeate flux and the foulant’s hydraulic resistance [9–11]. Fouling may be most simply modeled by employing a form of Darcy’s law,

$$J_w = \frac{\Delta P - \Delta \pi_m^*}{\mu (R_m + R_c)}, \quad (1)$$

where ΔP is the trans-membrane pressure drop (TMP), μ is the solution viscosity, $\Delta \pi_m^*$ is the cake-enhanced osmotic pressure [12], while R_m and R_c are the hydraulic resistances of the membrane and the foulant layer, respectively. Under most circumstances, little is known on the relation between the foulant mechanical properties and R_c , its observed hydraulic resistance.

Early viscometry-based studies already pointed out the relation between the foulant viscosity and its hydraulic resistance [13]. More recently, classical rheometry was used to analyze the bulk, macroscopic, mechanical properties and viscoelastic character of biofoulants [14,15], further pointing to the relation between the foulant layer rheology and its hydraulic resistance. Further, foulant layer properties measured using oscillatory rheometry and atomic force microscopy (AFM) were compared, highlighting some discrepancies between the micro and macro scale [16].

* Corresponding author.

E-mail address: ramong@technion.ac.il (G.Z. Ramon).

Experimentally, the macro-scale mechanical properties of calcium-alginate deposits developed on an RO membrane were characterized by employing an advanced rheometer in the parallel-plate mode [17]. This rheometry technique was later expanded to characterize membrane biofouling layers developing in membrane bioreactors [18], demonstrating the biofilm's dominant elastic character. Specifically, this solid-like behavior was more pronounced at high frequencies, while for low frequencies, or long time-scale deformations, the viscous term dominated. In a viscoelastic material, both viscous and elastic responses to applied stress can coexist, whereby the viscosity (liquid-like behavior) represents the resistance of the material to flow and the elasticity (solid-like behavior), describes the material's tendency for returning to its original shape once the applied stress is released. Furthermore, results showed that biofoulants can present a thixotropic and shear-thinning viscoelastic behavior with a yield stress [18]. The Quartz Crystal Microbalance with Dissipation (QCM-D) technique was also used to analyze the shear viscosity, and shear modulus of biofilms and their derivatives [19–21]. The results showed that the extra-cellular polymeric substances (EPS) play a major role in the biofilm's mechanical properties. This method also analyzed biofilm adherence, pointing to a clear correlation with its viscoelastic properties, and the corresponding membrane fouling rate. Moreover, this technique also revealed that Ca^{2+} can enhance or reduce the 'stiffness' of deposited EPS [22].

However, measuring foulant mechanical properties in-situ remains a challenge, since most of the current rheometry techniques are not suitable for measurement under filtration conditions. Being ex-situ in nature, and usually performed in 'autopsy'-style, following the experiment, such measurements may miss the actual mechanics of the foulant layer as it sustains various stresses from the pressure and, in particular, the permeation flow through it. Moreover, an important feature of in-situ measurements is the ability to determine the foulant hydraulic resistance and its rheology, simultaneously. Recently, optical coherence tomography (OCT) was used in-situ to analyze foulant structure, and reported a way to estimate the foulant bulk modulus by analyzing the overall porosity of the biofilm when subjected to compression and decompression tests [23]. In another OCT-based study, it was shown that biofoulants can exhibit a heterogeneous structure (concentration of biomass) at varying depth locations within the biofilm [24]. These findings demonstrate the presence of micro-scale variations of the mechanical properties, raising the question whether specific foulant regions dominate the influence on the observed hydraulic resistance.

In the present study, we aim to expand the ability to perform non-invasive, in-situ fouling analysis, demonstrating a new approach to measure the foulant's mechanical properties, based on a micro-rheological technique — a relatively new techniques for analyzing the micro-mechanics of soft matter. Microrheology may be considered 'passive' (as in the present work) or 'active', dependent on whether or not an external force is applied to the micro-scale tracers employed (e.g., using magnetic or optical tweezers) [25]. An advantage of this micro-scale analysis is its ability to provide information on local variations of the foulant microstructure. Meanwhile, a macroscale analysis (e.g., oscillatory rheometry) would show the foulant bulk rheology, an approach used extensively to investigate the mechanical properties of polymer gels [26–29] as well as biofilms at fluid interfaces [30]. However, it is currently not possible to perform such measurements under permeation conditions, limiting its use in the context of membranes or, indeed, other permeable systems.

In contrast, the micro-rheological method employed here allows in-situ analysis of the mechanical properties of a foulant, on the membrane surface, under varying filtration conditions.

Specifically, we aim to analyze the mechanical, visco-elastic properties of a deposited soft material, and connect these with the usually observed, 'macroscopic', properties such as the evolution of the pressure required to drive a given flux (in effect, the hydraulic resistance). Connecting the micro- and macro-scales can offer important mechanistic insight on fouling and its development under varying operational conditions, and lead to improved fouling control strategies.

2. Materials and methods

The experimental system is based on a direct-observation platform employing a custom-designed membrane flow-cell, enabling high-resolution, in-situ confocal microscopy [31,32]. Imaging of the foulant layer is facilitated via the addition of fluorescent-labeled micro-beads to the feed solution, which then become embedded in the deposited foulant layer, serving as tracers [33]. Tracer particle motion within the foulant layer is acquired using high frame-rate confocal imaging. The tracers' motion is captured in 2D, in the xy plane parallel to the membrane surface, and at a known distance from it. While acquiring images in the z-plane, perpendicular to the membrane, is also possible, the frame-rate of acquisition in the x–y plane is much higher, which is essential for resolving the fast vibrations of the tracer particles. The vibrations are a thermally-driven motion - a class of stochastic processes, of which Brownian motion is probably the best known. Specifically, the motion of the tracer is the result of the constant collisions experienced with surrounding molecules of the fluid in which the tracers are embedded. Since particle motion mostly occurs due to this thermal motion, 2D analysis in the xy plane is normally sufficient [25]. Following image acquisition, two computational steps are performed: (1) image processing and particle-tracking algorithms are employed to obtain the trajectories of particle motion, and (2) the tracers' ensemble-averaged, mean-squared-displacement (MSD) is calculated based on the particle trajectories. The MSD is then employed in the calculation of the mechanical properties of the foulant. A more detailed description of the experimental setup and the employed mechanical properties estimation is provided hereafter.

2.1. Experimental setup

The direct microscopic observation system consists of a membrane filtration flow-cell fitted with an optical window, which is placed on the stage of a laser-scanning confocal microscope (TCS SP8, Leica). The cell is connected to a pressurized feed vessel, with the source pressure adjusted by a feedback-controller (Fluigent MFCS-EZ) connected to a microfluidic flow sensor (Fluigent FRP), set to achieve the designated permeate flux. A schematic illustration of the experimental setup is shown in Fig. 1. The membrane employed for the experiments is a nanofiltration membrane (NF270, Dupont) with an effective filtration area of 2.16 cm² (dimensions: 0.6 mm (H) × 6 mm (W) × 36 mm (L)).

2.2. Model foulant

The model foulant used in the present study is alginate, a commonly-used model foulant [5,8,34] as it represents soft, gel-like deposits and extracellular polymeric substances (EPS), which play a crucial role in fouling and biofilm formation [19,35,36] and strongly influence the mechanical properties of biofilms [37]. The importance of alginate mechanical properties has been pointed out in the fouling literature [17,38]. Alginate consists of unbranched chains comprising two different types of homopolymeric blocks, namely β -D-Mannuronate (M-blocks) and α -L-Guluronate (G-blocks), potentially separated by regions of alternating structure (MG) [39]. Guluronate polymer blocks (G-blocks), in particular, can bind divalent cations conforming to an egg-box arrangement [40]. Aqueous alginate solutions, are known for their film-forming, thickening, mild gelation properties in the presence of divalent cations such as Ca^{2+} [41]. The homopolymeric G-Blocks provide gel-forming capacity, while MM and MG units offer flexibility. Thus the rigidity of chain blocks decreases along with the series GG > MM > MG [41].

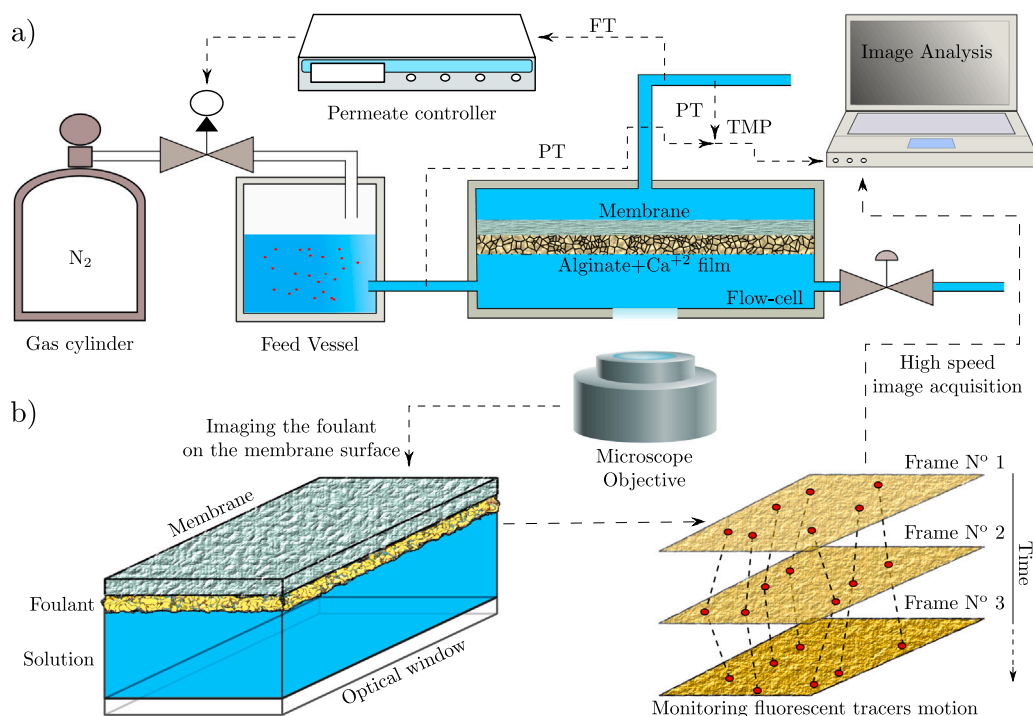


Fig. 1. (a) Schematic illustration of the experimental system. Here, FT and PT denote the flow and pressure transmitters, respectively, and TMP is the transmembrane pressure. (b) The bottom part of the schematic shows a close up view of the microscope imaging pathway, illustrating the scanning of particles at various distances from the membrane surface.

2.3. Experimental protocol

Before each experiment, the NF membrane coupon is placed in the flow-cell and its permeability is tested for deionized-water, while step changes are made to the applied pressure. Thereupon, the flow-cell containing the NF membrane is connected to the foulant feed system and mounted on the confocal microscope. Prior to each experiment, the feed solution is prepared in the feed-vessel by combining 200 mL de-ionized water with 11 mL alginate solution of 0.5 g/l Alginic acid sodium salt from brown algae (Sigma), providing an alginate concentration of ~ 36 mg/L in the feed solution. Further, 0.22 mL aqueous suspension of 0.5 μm diameter fluorescent polystyrene carboxylate-modified beads (Sigma) is added (yielding $\sim 1 \cdot 10^9$ particles/mL). Finally, a magnetic stirrer and an aqueous solution of calcium chloride anhydrous (Baker) is added to the feed solution, adjusted to obtain a calcium concentration of 1 mM. The feed solution is at a temperature of 25 °C, and has a pH of 4.9. The solution is freshly prepared 15 min before each experiment in order to prevent possible bulk gelation of alginate and calcium as well as possible aggregation of the fluorescent beads. The deposition of alginate+Ca²⁺ on the membrane surface is achieved under cross-flow filtration mode, using a rotameter to set the feed flowrate at 15 mL/min, equivalent to a crossflow velocity of ~ 0.07 m/s within the flow-cell.

In order to enable imaging, the flow-cell is mounted on the stage of the confocal microscope. To visualize the fluorescent particles, a 488 nm laser is employed, with a high-resolution objective (Fluotar VISIR 25 \times /0.95 WATER). A hybrid detector (HyD, Leica) is employed to capture the fluorescence emission of the particles, at wavelengths 510–672 nm. To visualize the position of the membrane surface, we capture the 488 nm laser deflection, employing photo-multiplier tubes (PMT). In order to determine the precise location of the scanned foulant layers in terms of their distance from the membrane surface, we first set the ‘0-plane’ based on the laser reflected from the membrane surface, by scanning with the confocal and seeking the plane of maximum intensity. Once the membrane position is determined, stage-stepping (with nanometer precision) is made by the confocal microscope to the

desired location. In this fashion, the focal plane in which 2D scans are collected is at the indicated distance from the membrane. The employed fluorescent particles embedded in the foulant layer are assumed to undergo minimal interaction with the alginate layer at the pressure and flow conditions examined here. However, we note that the impact of surface properties of particles employed for micro-rheology is the subject of an ongoing research in the fields of soft matter and colloid physics [42].

Following 50 min of foulant deposition, the feed and concentrate valves are closed, and the feed is switched to double-deionized water, replacing the alginate solution. This is done in order to facilitate the subsequent imaging of the system under varying permeation rates, in a way that ensures that no changes to the foulant layer will be caused by further accumulation of the foulant. Therefore, image acquisition for particle tracking, is made while DI water is used as the feed. For flux-stepping, the controller is set to the pressure required to fix the permeate fluxes at values of 2, 4, and 8 $\mu\text{m/s}$ (7.2, 14.4, and 28.8 LMH, respectively). The micro-rheology measurements are performed once the TMP reaches an apparent steady-state condition, which implies that relaxation of the alginate layer has been achieved. For each experiment, three different locations along the fouled membrane are scanned, each at a distance of 30, 60, and 90 μm measured from the membrane surface into the deposited foulant layer.

2.4. Multiple particle tracking and calculation of mechanical properties

For particle-tracking based on image analysis of the acquired confocal images, we employed a modified version of the code written for IDL by Crocker and Grier [43]. Once particle trajectories are obtained, the mean square displacement (MSD) is calculated in 2-dimensions, using

$$\langle \Delta r^2(\tau) \rangle = \left\langle \left| x(t_i + \tau) - x(t_i) \right|^2 + \left| y(t_i + \tau) - y(t_i) \right|^2 \right\rangle, \quad (2)$$

where x and y are the tracer position coordinates in the visualized plane. The subscript i in t_i denotes the frame number. The parameter τ represents the lag time between two consecutive positions, thus

mapping the tracer displacements for different time-lapses, where for video microscopy the minimum lag time is $\tau_{\min} = 1/f$, where f is the acquisition frame-rate and also the upper-limit of the analyzed frequency spectrum of mechanical response. Here, the notation $\langle \rangle$ denotes an ensemble-average computed over several tracer trajectories.

The thermally-driven trajectories of particles embedded in a viscoelastic medium may be related to the diffusion coefficient, D , and complex viscosity, η , via the Generalized Einstein–Stokes relation (GSER) [43–45]. The GSER describes how the diffusion coefficient of a micro-particle embedded in a fluid correlates with the particle’s stochastic, thermal-driven motion, which is resisted by the drag exerted on the particle during its motion. The material is assumed to be linearly visco-elastic, and its mechanical properties have been derived from the stochastic equation of motion (the Langevin equation) by Mason and Weitz [46], to yield

$$\tilde{G}(s) = \frac{k_b T}{\pi a s \langle \Delta \tilde{r}^2(s) \rangle}, \quad (3)$$

in which $\tilde{G}(s)$ is the viscoelastic spectrum and $\tilde{\cdot}$ denotes the (unilateral) Laplace transform, a is the particle radius, T is the temperature of the fluid, k_b is the Boltzmann constant and s represents the frequency in the Laplace-transformed domain. In our calculations, we employ an approximation derived by Mason [47], given by

$$|G^*(\omega)| \approx \frac{k_b T}{\pi a \left\langle \Delta r^2 \left(\frac{1}{\omega} \right) \right\rangle \Gamma [1 + \alpha(\omega)]}, \quad (4)$$

in which $G^*(\omega)$ is the frequency-dependent complex shear modulus. Here, Γ is the gamma function, and α is the logarithmic derivative of the MSD in time,

$$\alpha(\omega) = \left. \frac{d \ln \langle \Delta r^2(\tau) \rangle}{d \ln t} \right|_{\tau=1/\omega}, \quad (5)$$

which varies between zero, for a purely elastic medium, and unity, in the case of a Newtonian, viscous fluid. The two moduli, $G'(\omega)$ and $G''(\omega)$, represent the storage (elastic) and loss (viscous) moduli, respectively, and are functions of the frequency, ω , describing the material response to an imposed oscillatory stress. For example, a non-Newtonian material can exhibit a viscous-like response for low frequencies, manifested as a higher value of the loss modulus compared with the storage modulus. However, the same material can exhibit an elastic solid-like response at higher frequencies, where mechanical properties are dominated by the storage modulus. Hence, for frequency-dependent materials, this data is useful for predicting material response when deformed over short (high frequencies) or long (low frequencies) time scales. The elastic and viscous parts of the complex modulus, $G'(\omega)$ and $G''(\omega)$ are connected via the Kramers–Kronig relations, where the real part of a Fourier-transformed causal function determines its imaginary part and vice-versa, and we calculate both moduli as follows:

$$\begin{aligned} G'(\omega) &= |G^*(\omega)| \cos \left(\frac{\pi \alpha(\omega)}{2} \right), \\ G''(\omega) &= |G^*(\omega)| \sin \left(\frac{\pi \alpha(\omega)}{2} \right). \end{aligned} \quad (6)$$

3. Results and discussion

3.1. Tracer motion and confinement within the foulant layer

We now turn to examine the main output of the visualization experiments — the particle trajectories and their implications. To illustrate the qualitatively different behavior of particles in the system, Fig. 2a shows a representative 3D reconstruction of the confocal imaging made during foulant deposition. In the image, the membrane surface appears in green and the tracer particles are red dots. Notably, some of the particles appear to be stationary, while others are in motion — seen as

‘smeared’ dotted lines at the top of the image. The (seemingly) stationary particles mark the region occupied by the alginate layer, in which they are embedded, while the moving particles are carried with the flow outside the foulant layer. This is a clear illustration of the different character of the two layers, schematically shown on the bottom-left panel of Fig. 2a, demarcating particles at different locations in the image: embedded at different depths (1 — at 30 μm , 2 — at 90 μm) and 3 — moving with the flow, outside the deposited foulant. On the bottom-right panel of Fig. 2a, a cross-section cryogenic electron-microscopy image (cryo-SEM) is shown, illustrating the typical hydrogel structure of the alginate [48,49], as well as an embedded particle. Further images obtained using cryo-SEM, and some basic details of the method, are shown in Figs S1 and S2 of the supplementary material.

The trajectories of the particles, as may be seen in Fig. 2b, exhibit very different characteristics when in the free-flowing stream (particle 3) or embedded in the alginate deposit (particles 1 and 2). In particular, particles (1) and (2) are clearly confined in their motion, albeit to a varying extent. This is an important difference, which reflects the variation in their surrounding medium at different locations within the foulant layer. Specifically, in this particular case (permeate flux $J_w = 8 \mu\text{m/s}$, or $\sim 28 \text{ LMH}$), particle (1), located 30 μm from the membrane, is clearly more “caged” than particle (2), which is at a distance of 90 μm from the membrane.

Next, the trajectories of the alginate-embedded particles are used to calculate the ensemble-averaged MSDs, shown in Fig. 2c. The more confined the particle motion is, the lower the slope of the MSD curve will be. This behavior is often characterized by the anomalous diffusion exponent, β (appearing in the relation $\text{MSD} \propto D^\beta t$), where sub-diffusive behavior would exhibit $\beta < 1$, as occurs for these two particles; this is shown in contrast with the purely Brownian motion, for which $\beta = 1$. Furthermore, in the case shown, the MSD of particle 2 is larger than that of particle 1 — this can be observed in Fig. 2b, represented by the area over which the particle trajectory extends — the MSD provides a quantitative indication of this.

3.2. Micro-scale rheological properties of the foulant

Next, we turn to examine the mechanical properties of the foulant layer, namely the storage (G') and loss (G'') moduli, computed based on the MSDs, averaged over multiple particles. Specifically, the analysis is made using images acquired at different depths within the layer (30, 60, and 90 μm from the membrane surface), in order to reflect the spatial variation of the layer structure. The foulant layer in the forthcoming analysis was measured to have a thickness of $\sim 100 \mu\text{m}$ (based on the average location of particles seen at the furthest location from the membrane), such that the three chosen depths form a representative distance distribution. The calculated moduli are shown in Fig. 3, illustrating the foulant layer’s rheological response to variations in the permeate flux, J_w , imposed on the system (2, 4, and 8 $\mu\text{m/s}$). In particular, the frequency response of the storage and loss moduli is shown, extracted from the stochastic motion of the fluorescent beads captured by the microscope. In contrast to other rheology methods, this passive method does not rely on imposing an external stress while monitoring the mechanical response of the material, in terms of the applied frequency, e.g., as in oscillatory rheometry. A full experimental dataset, including 3 membrane locations, each scanned at 3 depths, is shown in Fig. S5 of the supplementary material.

The mechanical properties of the foulant exhibit a dominance of the elastic component, G' , over the viscous part, G'' , for the entire spectrum of analyzed frequencies. The elastic modulus is generally associated with the degree of material crosslinking, which in the present case occurs due to Ca^{2+} interactions with alginate [40]. These results, obtained at the micro-scale, agree well with macro-scale measurements of dilute calcium-alginate gels, employing oscillatory rheometry [38] (the gel structure, as seen in Fig. S1 and Fig. S2, also reflects the structure of a typical heterogeneous hydrogel). However, our measurement further

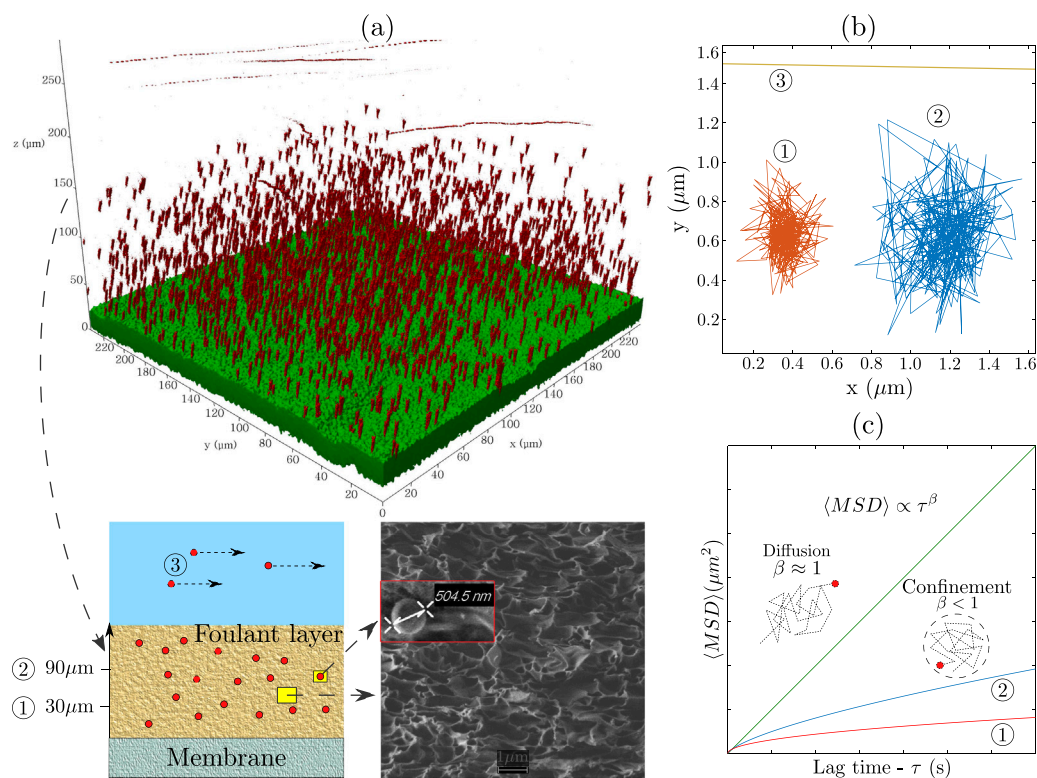


Fig. 2. (a) Fouling deposition stage monitored using confocal microscopy. The tracer particles and the NF membrane are displayed in red and green, respectively. In the bottom-left is an illustration of the analyzed foulant layers. In the bottom-right, a cryo-SEM image of the deposited alginate cross-section and, in the inset, an embedded tracer. (b) The particle trajectories of three 0.5 μm fluorescent tracer beads, at two different alginate depths, marked as locations (1) and (2), 30 and 90 μm away from the membrane surface, respectively, and location (3), representing free particles in the flow stream, outside the foulant layer. (c) Illustration of the MSD behavior for different types of tracer motion.

reveals an intricate material response due to the imposed changes of the permeate flux, a unique feature of this system, observed at both depth locations within the foulant layer. In the case considered here, multiple effects may manifest to varying degrees, all affected by the filtration conditions. First, pressure applied on the foulant may result in compaction, while the flow through the layer exerts a shear stress. Furthermore, the local ionic composition may yield variations in material properties, and is impacted by permeation via concentration polarization. These are discussed further in a later section.

To facilitate a more straightforward interpretation of the measured mechanical properties, we extract the storage modulus at a frequency of 0.2 Hz, which represents long-time relaxation of the layer, and present the corresponding $G'(0.2 \text{ Hz})$, measured for different permeate fluxes (2, 4, and 8 μm/s) and at varying depths (see Fig. 4). The results indicate that the $G'(0.2 \text{ Hz})$ value of the foulant decreases as one moves further away from the membrane surface, and this is most strongly observed for low flux. The observed trend becomes increasingly non-linear as the permeate flux increases, as manifested in a decreased lack-of-fit test (LOF) p -value in a linear regression of $G'(0.2 \text{ Hz})$ vs. J_w (see Fig. 4), possibly indicating that the viscous drag force induced by permeation, and resultant material deformation, is less significant for low permeate fluxes [50–52]. At higher permeate fluxes (and TMPs), the force due to the pressure drop across the layer may affect its structure and stiffness due to compaction, manifested in the observed non-linear pressure–flux response.

Another possible reason for the spatial variation of the foulant layer properties, also flux-dependent, might be the distribution of Ca^{2+} within the layer, (we recall that Ca^{2+} acts as a crosslinker and so its presence modifies the micromechanics of the alginate). Specifically, we speculate that the initial calcium concentration profile may be influenced by cake-enhanced concentration polarization (CP) [12] (see illustration in Fig. S6). Furthermore, during the flux stepping experiments, some Ca^{2+} present in the alginate between M-blocks and

GM-blocks may be displaced towards the membrane surface as the flux is increased, since Ca^{2+} interaction in the alginate is dominated by G-blocks [40,41]. This would, again, result in a strongly polarized concentration profile that modifies the local mechanical properties of the layer, in addition to the stresses exerted by the permeate flux and the TMP, ultimately creating a complex interdependence reflected in the micro-rheological measurement. In addition, the shift to DIW may partially flush the sodium cations present in the deposited alginate matrix, affecting the calcium alginate gelation [53–55]. As we cannot provide direct evidence of these ion transport effects, they remain speculative within the present context, but pose interesting questions for future work on the CP layer within deposited hydrogels. However, we note that such measurements are non-trivial and, furthermore, a large uncertainty is always present with respect to actual chemical composition of a foulant layer, in-situ. The importance of the analysis demonstrated here is in the real-time observation of foulant layer dynamics, even under limited certainty regarding its chemical composition and, hence, exact structure. Our findings show that the degree of confinement, as observed in the average motion of tracers, varies over z (see Fig. 2b) indicating depth variations in the mobility and the storage modulus (elastic component) of the foulant, as shown in Fig. 4.

3.3. Linking the micro- and macro-scale observations

An important consequence of our methodology is the ability to link macroscopic system characteristics, for example, TMP variations at a given imposed flux, with microscale structure and mechanics. In the experiments, when the flux was increased step-wise, variations of the foulant layer hydraulic resistance were observed over time (see Fig. 6a). Bearing in mind that the employed experimental method is set so as to avoid further foulant deposition during the analysis, we may attribute the observed variations to the foulant rheological response to the new operational conditions imposed at each step. We

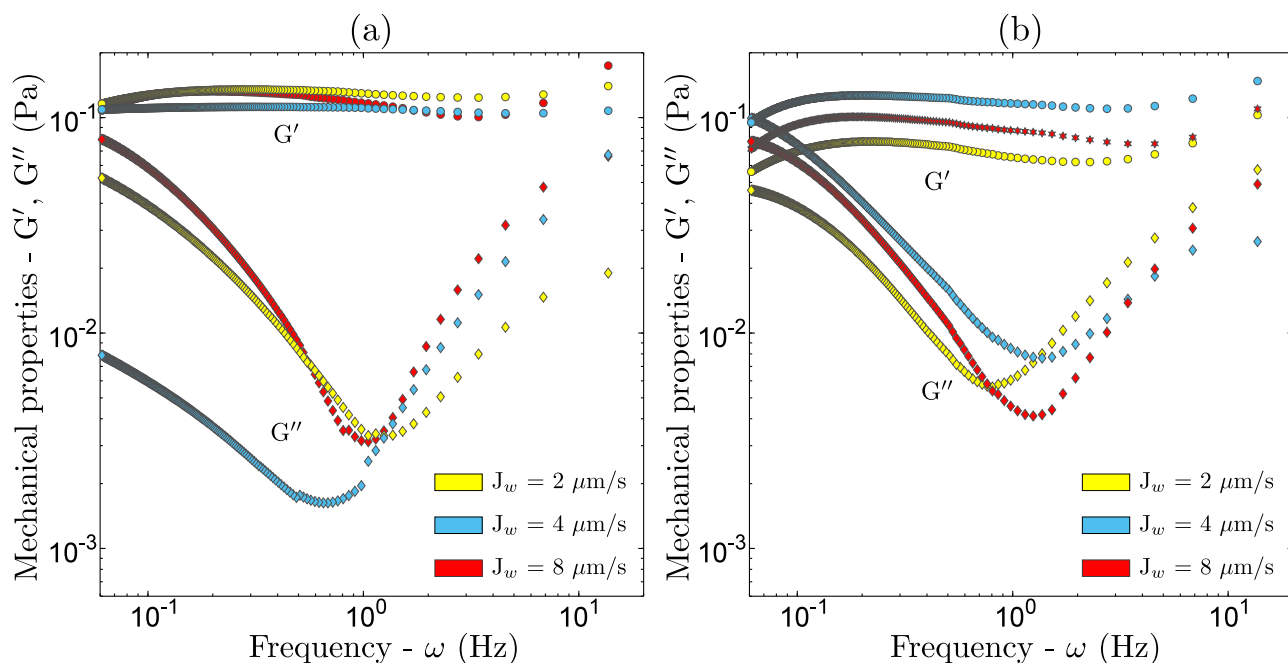


Fig. 3. The measured mechanical properties of the foulant layer under different permeate fluxes, measured at distances of (a) 30 μm and (b) 90 μm from the membrane surface. The yellow, blue and red datapoints represent the foulant properties measured at fluxes of 2, 4, and 8 $\mu\text{m/s}$, respectively (7.2, 14.4, and 28.8 LMH). The storage (G') and loss (G'') moduli of the foulant are shown as circles and diamonds, respectively.

also compare macro- and micro-scale observations through the analysis of three alginate deposits that exhibited different hydraulic resistances. Specifically, their micro-rheology was measured at a distance of 30 μm from the membrane surface and compared with the observed hydraulic resistance (or the required TMP to achieve the imposed permeate fluxes). The analyzed alginate deposits had a similar thickness, ranging between 80–100 μm , but required different TMPs in order to impose the required permeate flux during the experiment (see Fig. 5a). Fig. 5a shows the variation of TMP in time for $J_w = 2, 4$ and 8 $\mu\text{m/s}$ (7.2, 14.4, and 28.8 LMH). The red and yellow curves represent two experiments

where a TMP of 2 bar was applied during the shift from the alginate solution to DIW, while the blue curve shows an experiment where the TMP was 0 during the shift. This variation was found to affect the foulant layer’s hydraulic resistance. In contrast to the observed variations in hydraulic resistance, we did not observe variations in the final deposited layer thickness.

The TMP required to drive a flux of 2 $\mu\text{m/s}$ exhibited no significant difference between the various experiments, with a small interquartile range (IQR), see Fig. 6a, and almost no difference between the lower and upper IQR. However, the distribution of the required TMP variation between the experiments increased proportionally to J_w , with a corresponding increased IQR. It is also worth noting that the foulant’s hydraulic resistance increased in proportion to the time required to reach an apparent steady TMP, following a step increase of the permeate flux, see Fig. 5a. The blue curve in Fig. 5a, shows the lowest TMPs and very rapid relaxation (time required to reach steady-state), while the yellow curve presented the highest TMPs and a highly non-linear trend of the transient TMP.

Also shown in Fig. 5b is the complex viscosity, $(|\eta^*|(\omega))$, measured at 30 μm from the membrane surface, in the same set of experiments discussed above. Interestingly, the complex viscosity has the lowest values for conditions that presented the lowest hydraulic resistance (or required TMP). Furthermore, under these conditions, a decrease in the complex viscosity is seen upon increasing the permeate flux (see the blue hexagonal data points in 5b). In contrast, conditions leading to higher hydraulic resistance show a much less pronounced decrease in their complex viscosity at higher permeate flux.

In order to link microscopic characteristics with macroscopic system behavior, Fig. 6b shows the values of $G'(0.2 \text{ Hz})$ measured at different distances from the membrane, z , vs. the foulant hydraulic resistance calculated from the measured TMP at each set value of J_w . For the three analyzed permeate fluxes of 2, 4 and 8 $\mu\text{m/s}$ (7.2, 14.4, and 28.8 LMH, respectively), the hydraulic resistances were 3.6×10^{13} , 74.5×10^{13} , and $131.2 \times 10^{13} \text{ (m}^{-1}\text{)}$, respectively. The data suggests that the storage modulus varies more strongly with z when the permeate and TMP are increased. A linear regression of the data reveals a small increase of $G'(0.2 \text{ Hz})$ at 30 μm when increasing the permeate flux. Also, the LOF for the regressions exhibits a decreasing p -value at increased foulant

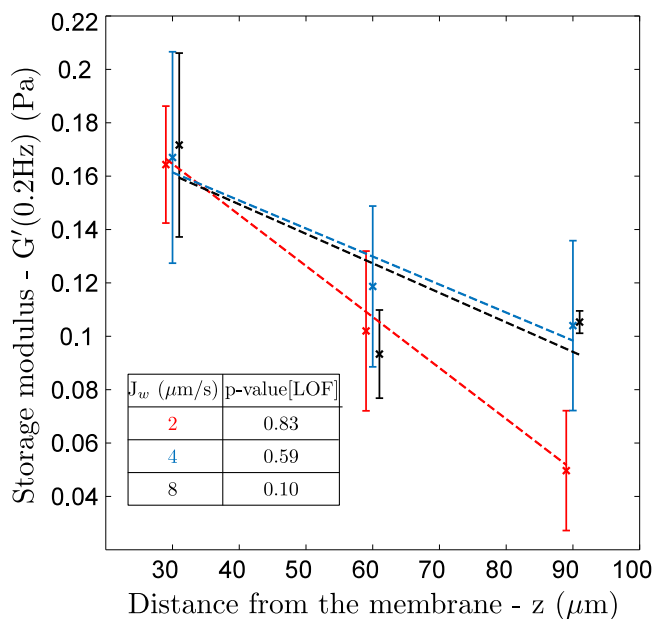


Fig. 4. The long-time storage modulus, G' (at a frequency of 0.2 Hz), as measured at varying distances from the membrane surface, under permeate fluxes of 2, 4, and 8 $\mu\text{m/s}$ (7.2, 14.4, and 28.8 LMH), shown in red, blue, and black, respectively.

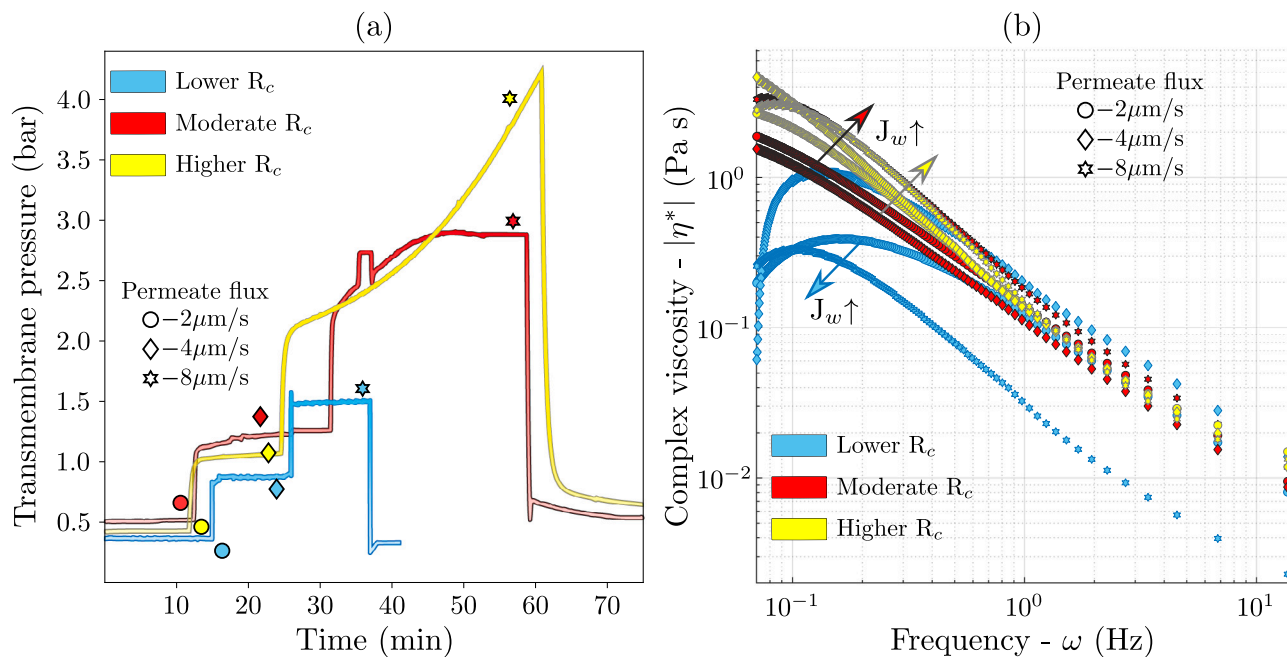


Fig. 5. (a) The foulant complex viscosity modulus, $|\eta^*|$ measured at $30 \mu\text{m}$ from the membrane surface, under three different operational conditions during the deposition stage. (b) The time-variation of the TMP required to achieve the designated permeate flux for each experiment.

depth, indicating a non-linear increase of $G'(0.2 \text{ Hz})$ with z . The results show that $G'(0.2 \text{ Hz})$ values within the foulant, which represent its long-time elastic response, are sensitive to J_w , and are particularly dependent on the distance from the membrane surface. Moreover, the foulant layer located at the largest distance from the membrane surface ($90 \mu\text{m}$) exhibits the highest local variations in mechanical properties in response to changes in J_w . This is in contrast to the foulant layer located at a distance of $30 \mu\text{m}$ from the membrane surface, which showed a much lower variation in $G'(0.2 \text{ Hz})$ when the permeation rate, J_w , was increased. The data displayed in Fig. 6b corresponds with the data displayed in red for Fig. 5a. We note that, while we attempt to identify the main mechanisms at play, there is likely to be some overlap and possibly some competition between the effects imparted via compressive stresses applied by the feed pressure, the shear stress imparted by J_w , the displacement of calcium cations by convection [56], and due to CP.

3.4. The response of the foulant layer to operational parameters

Aqueous solutions of calcium alginate have been previously characterized as having thixotropic behavior [57], meaning that under an applied shear stress, a decreased viscosity is observed along shearing time. The opposite behavior corresponds with a rheopectic material. Generally speaking, the foulant deposited on the membrane surface is subject to compaction by both the applied pressure and shear stress exerted by the flow through the layer. Immediately following the TMP increase (adjusted by the controller so as to maintain the designated J_w), two antagonistic rheological responses may arise within the foulant layer: ‘stiffening’ due to compression of the layer, and the shear-induced ‘softening’ by the permeation flow. Interestingly, our results resemble those obtained through standard compression tests, which exhibited stiffening of both alginate and calcium alginate solutions [58–60]. In the system considered here, however, the rheological responses to compression and shear are coupled. Our results suggest that the variation in the foulant complex viscosity due to compaction (see Fig. 5b),

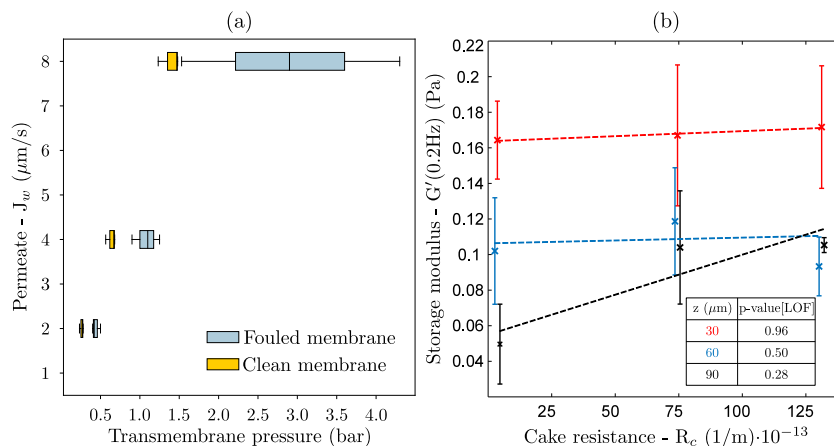


Fig. 6. (a) The steady-state TMP required to achieve the target permeate fluxes (J_w). The boxes represent the interquartile range (IQR). (b) The long-time storage (elastic) modulus, $G'(0.2 \text{ Hz})$, vs. the observed foulant hydraulic resistances. In both figures, Lack-of-Fit (LOF) tests are shown for each set of data, based on linear regressions for the selected parameter.

dominates over that due to the shear stress exerted by the permeate flux. In particular, the complex viscosity increases as the permeate flux increases (stiffening), which is manifested in a correspondingly higher hydraulic resistance (see red and yellow curves in Fig. 5). The exceptions to this trend are the samples with the lowest hydraulic resistance, which exhibited softening of the layer at the highest permeate flux, indicating that the response to permeation-induced shear dominated over the compaction due to the TMP. These findings are in some agreement with a relatively recent published theory on biofilm rheology, which suggested that the biofilm stiffens by compression and softens by shear stress [61].

Lastly, our micro-scale results highlight the frequency-dependent mechanical properties of the studied foulant layer. The observed connection between the foulant's frequency-dependent mechanical properties and its hydraulic resistance, R_c , shares an interesting resemblance with recent measurements using 'hydraulic impedance' [62], which involved imposing a sinusoidal permeate flux through a membrane, fouled with calcium alginate, while monitoring the periodic response of the TMP. As shown in that work, at higher frequencies, the deposit was more permeable [62]. This observation suggests, in light of our own measurements, that relaxation times and, consequently, 'stiffening' of the deposit or, conversely, shear-induced 'softening' of the material are reflected in the permeability of the material.

4. Conclusions

In this study we have applied microscopy-based particle tracking for monitoring the mechanical response of a model foulant to changes in operating conditions. The methodology enables in-situ, real time characterization of this response, providing a much needed link between macroscopically observed flux-pressure relations and micro-scale events occurring near the membrane surface.

Our results reveal that the foulant mechanical properties are more sensitive to changes in the permeate flux, within regions of the layer that are further away from the membrane. Meanwhile, the region closest to the membrane surface was stiffer, manifested through a higher value of the long-time elastic modulus and complex viscosity. Results further showed a positive correlation between the foulant's complex viscosity and its hydraulic resistance.

An important capability of the presented method is access to the frequency response of the material, as demonstrated on the viscoelastic calcium-alginate layers examined here. Future extensions of the presented methodology include applying the measured frequency response of a foulant layer, as a potential pathway for tuning back-pulsing such that the mechanical resistance of the layer is in-tune with the applied stress, for maximal removal efficiency.

Similarly, a frequency-dependent foulant may exhibit a variation in its capacity to be deformed and removed by a properly-tuned, sinusoidal crossflow shear. Overall, improved in-situ understanding of the foulant layer mechanical properties, as demonstrated here, may be key to successful control strategies and opens interesting prospects for future research.

List of symbols

Latin letters

| | |
|--------------|---|
| a | Particle radius [μm] |
| $ G^* $ | Complex modulus [Pa] |
| G' | Storage (elastic) modulus [Pa] |
| G'' | Loss (viscous) modulus [Pa] |
| J_w | Permeate flux [$\mu\text{m/s}$] |
| k_b | Boltzmann's constant [J/K] |
| ΔP | Transmembrane pressure (TMP) [bar] |
| Δr^2 | Mean squared displacement (MSD) [μm^2] |
| R_c | Foulant cake hydraulic resistance [m^{-1}] |
| R_m | Membrane hydraulic resistance [m^{-1}] |
| s | Frequency in the Laplace domain |
| t | Time [s] |
| T | Temperature [K] |
| x, y | Coordinates in a plane parallel to the membrane surface [μm] |
| z | Distance from the membrane surface [μm] |

Greek letters

| | |
|-----------------|---|
| α | Logarithmic derivative of the MSD in time |
| β | Anomalous diffusion exponent |
| $ \eta^* $ | Complex viscosity modulus [Pa s] |
| μ | Dynamic viscosity at the bulk [Pa s] |
| $\Delta\pi_m^*$ | Cake-enhanced osmotic pressure [bar] |
| τ | Lag time [s] |
| ω | Frequency [Hz] |

CRedit authorship contribution statement

José A. Epstein: Conceptualization, Methodology, Software, Formal analysis, Investigation, Data curation, Writing - original draft, Writing - review & editing, Visualization. **Guy Z. Ramon:** Conceptualization, Methodology, Resources, Validation, Writing - original draft, Writing - review & editing, Visualization, Funding acquisition.

Declaration of competing interest

One or more of the authors of this paper have disclosed potential or pertinent conflicts of interest, which may include receipt of payment, either direct or indirect, institutional support, or association with an entity in the biomedical field which may be perceived to have potential conflict of interest with this work. For full disclosure statements refer to <https://doi.org/10.1016/j.memsci.2021.119747>. Guy Ramon reports financial support, administrative support, and equipment, drugs, or supplies were provided by Technion Israel Institute of Technology. Jose Epstein reports financial support, administrative support, and equipment, drugs, or supplies were provided by Technion Israel Institute of Technology.

Acknowledgment

The research was supported by the Israel Science Foundation, grant number 2018/17.

Appendix A. Supplementary data

Supplementary material related to this article can be found online at <https://doi.org/10.1016/j.memsci.2021.119747>.

References

- [1] Y. Long, G. Yu, L. Dong, Y. Xu, H. Lin, Y. Deng, X. You, L. Yang, B.Q. Liao, Synergistic fouling behaviors and mechanisms of calcium ions and polyaluminum chloride associated with alginate solution in coagulation-ultrafiltration (UF) process, Water Res. 189 (2021) 116665, <http://dx.doi.org/10.1016/j.watres.2020.116665>.

- [2] Y. Xiao, W. Zhang, Y. Jiao, Y. Xu, H. Lin, Metal-phenolic network as precursor for fabrication of metal-organic framework (MOF) nanofiltration membrane for efficient desalination, *J. Membr. Sci.* 624 (2021) 119101, <http://dx.doi.org/10.1016/j.memsci.2021.119101>.
- [3] Z. Huang, J. Liu, Y. Liu, Y. Xu, R. Li, H. Hong, L. Shen, H. Lin, B.Q. Liao, Enhanced permeability and antifouling performance of polyether sulfone (PES) membrane via elevating magnetic Ni@MXene nanoparticles to upper layer in phase inversion process, *J. Membr. Sci.* 623 (2021) <http://dx.doi.org/10.1016/j.memsci.2021.119080>.
- [4] Y. Xu, Y. Xiao, W. Zhang, H. Lin, L. Shen, R. Li, Y. Jiao, B.Q. Liao, Plant polyphenol intermediated metal-organic framework (MOF) membranes for efficient desalination, *J. Membr. Sci.* 618 (2021) 118726, <http://dx.doi.org/10.1016/j.memsci.2020.118726>.
- [5] H.C. Kim, B.A. Dempsey, Membrane fouling due to alginate, SMP, EfOM, humic acid, and NOM, *J. Membr. Sci.* 428 (2013) 190–197, <http://dx.doi.org/10.1016/j.memsci.2012.11.004>.
- [6] C. Dreszer, A.D. Wexler, S. Drusová, T. Overdijk, A. Zwijnenburg, H.C. Flemming, J.C. Kruijthof, J.S. Vrouwenvelder, In-situ biofilm characterization in membrane systems using optical coherence tomography: Formation, structure, detachment and impact of flux change, *Water Res.* 67 (2014) 243–254, <http://dx.doi.org/10.1016/j.watres.2014.09.006>.
- [7] S.T. Kang, A. Subramani, E.M. Hoek, M.A. Deshusses, M.R. Matsumoto, Direct observation of biofouling in cross-flow microfiltration: Mechanisms of deposition and release, *J. Membr. Sci.* 244 (1–2) (2004) 151–165, <http://dx.doi.org/10.1016/j.memsci.2004.07.011>.
- [8] K. Katsoufidou, S.G. Yiantsios, A.J. Karabelas, Experimental study of ultrafiltration membrane fouling by sodium alginate and flux recovery by backwashing, *J. Membr. Sci.* 300 (1–2) (2007) 137–146, <http://dx.doi.org/10.1016/j.memsci.2007.05.017>.
- [9] X. Zhu, M. Elimelech, Colloidal fouling of reverse osmosis membranes: Measurements and fouling mechanisms, *Environ. Sci. Technol.* 31 (12) (1997) 3654–3662, <http://dx.doi.org/10.1021/es970400v>.
- [10] A. Seidel, M. Elimelech, Coupling between chemical and physical interactions in natural organic matter (NOM) fouling of nanofiltration membranes: Implications for fouling control, *J. Membr. Sci.* 203 (1–2) (2002) 245–255, [http://dx.doi.org/10.1016/S0376-7388\(02\)00013-3](http://dx.doi.org/10.1016/S0376-7388(02)00013-3).
- [11] D.J. Miller, S. Kasemset, D.R. Paul, B.D. Freeman, Comparison of membrane fouling at constant flux and constant transmembrane pressure conditions, *J. Membr. Sci.* 454 (2014) 505–515, <http://dx.doi.org/10.1016/j.memsci.2013.12.027>.
- [12] E.M. Hoek, M. Elimelech, Cake-enhanced concentration polarization: A new fouling mechanism for salt-rejecting membranes, *Environ. Sci. Technol.* 37 (24) (2003) 5581–5588, <http://dx.doi.org/10.1021/es0262636>.
- [13] J.L. Harris, Influence of gel layer rheology on ultrafiltration flux of wheat starch effluent, *J. Membr. Sci.* 29 (1) (1986) 97–109, [http://dx.doi.org/10.1016/S0376-7388\(00\)82021-9](http://dx.doi.org/10.1016/S0376-7388(00)82021-9).
- [14] B.W. Towler, C.J. Rupp, A.L. Cunningham, P. Stoodley, Viscoelastic properties of a mixed culture biofilm from rheometer creep analysis, *Biofouling* 19 (5) (2003) 279–285, <http://dx.doi.org/10.1080/0892701031000152470>.
- [15] A. Houari, J. Picard, H. Habarou, L. Galas, H. Vaudry, V. Heim, P. Di Martino, Rheology of biofilms formed at the surface of NF membranes in a drinking water production unit, *Biofouling* 24 (4) (2008) 235–240, <http://dx.doi.org/10.1080/08927010802023764>.
- [16] A. Safari, Z. Tukovic, M. Walter, E. Casey, A. Ivankovic, Mechanical properties of a mature biofilm from a wastewater system: from microscale to macroscale level, *Biofouling* 31 (8) (2015) 651–664, <http://dx.doi.org/10.1080/08927014.2015.1075981>.
- [17] D.C. Sioutopoulos, T.B. Goudoulas, E.G. Kastrinakis, S.G. Nychas, A.J. Karabelas, Rheological and permeability characteristics of alginate fouling layers developing on reverse osmosis membranes during desalination, *J. Membr. Sci.* 434 (2013) 74–84, <http://dx.doi.org/10.1016/j.memsci.2013.01.018>.
- [18] S.I. Patsios, T.B. Goudoulas, E.G. Kastrinakis, S.G. Nychas, A.J. Karabelas, A novel method for rheological characterization of biofouling layers developing in membrane bioreactors (MBR), *J. Membr. Sci.* 482 (2015) 13–24, <http://dx.doi.org/10.1016/j.memsci.2015.02.016>.
- [19] O. Orgad, Y. Oren, S.L. Walker, M. Herzberg, The role of alginate in *Pseudomonas aeruginosa* EPS adherence, viscoelastic properties and cell attachment, *Biofouling* 27 (7) (2011) 787–798, <http://dx.doi.org/10.1080/08927014.2011.603145>.
- [20] A. Sweity, W. Ying, M.S. Ali-Shtayah, F. Yang, A. Bick, G. Oron, M. Herzberg, Relation between EPS adherence, viscoelastic properties, and MBR operation: Biofouling study with QCM-d, *Water Res.* 45 (2011) 6430–6440, <http://dx.doi.org/10.1016/j.watres.2011.09.038>.
- [21] D. Ferrando, C. Ziemba, M. Herzberg, Revisiting interrelated effects of extracellular polysaccharides during biofouling of reverse osmosis membranes: Viscoelastic properties and biofilm enhanced osmotic pressure, *J. Membr. Sci.* 523 (2017) 394–401, <http://dx.doi.org/10.1016/j.memsci.2016.08.071>.
- [22] D. Ferrando, D. Toubiana, N.S. Kandiyote, T.H. Nguyen, A. Nejjad, M. Herzberg, Ambivalent role of calcium in the viscoelastic properties of extracellular polymeric substances and the consequent fouling of reverse osmosis membranes, *Desalination* 429 (2018) 12–19, <http://dx.doi.org/10.1016/j.desal.2017.12.006>.
- [23] S. Kerdi, A. Qamar, A. Alpatova, N. Ghaffour, An in-situ technique for the direct structural characterization of biofouling in membrane filtration, *J. Membr. Sci.* 583 (2019) 81–92, <http://dx.doi.org/10.1016/j.memsci.2019.04.051>.
- [24] J. Hou, C. Wang, R.T. Rozenbaum, N. Gusanari, E.D. de Jong, W. Woudstra, G.I. Geertsema-Doornbusch, J. Atema-Smit, J. Sjollema, Y. Ren, H.J. Busscher, H.C. van der Mei, Bacterial density and biofilm structure determined by optical coherence tomography, *Sci. Rep.* 9 (1) (2019) <http://dx.doi.org/10.1038/s41598-019-46196-7>.
- [25] E.M. Furst, T.M. Squires, *Microrheology*, Oxford University Press, 2017, <http://dx.doi.org/10.1093/oso/9780199655205.001.0001>.
- [26] J. Apgar, Y. Tseng, E. Fedorov, M.B. Herwig, S.C. Almo, D. Wirtz, Multiple-particle tracking measurements of heterogeneities in solutions of actin filaments and actin bundles, *Biophys. J.* 79 (2) (2000) 1095–1106, [http://dx.doi.org/10.1016/S0006-3495\(00\)76363-6](http://dx.doi.org/10.1016/S0006-3495(00)76363-6).
- [27] M.T. Valentine, P.D. Kaplan, D. Thota, J.C. Crocker, T. Gisler, R.K. Prud'homme, M. Beck, D.A. Weitz, Investigating the microenvironments of inhomogeneous soft materials with multiple particle tracking, *Phys. Rev. E* 64 (6) (2001) 9, <http://dx.doi.org/10.1103/PhysRevE.64.061506>.
- [28] T. Moschakis, *Microrheology and particle tracking in food gels and emulsions*, *Curr. Opin. Colloid Interface Sci.* 18 (4) (2013) 311–323, <http://dx.doi.org/10.1016/j.cocis.2013.04.011>.
- [29] J. Fernandez-Castanon, S. Bianchi, F. Saglimbeni, R. Di Leonardo, F. Sciortino, *Microrheology of DNA hydrogel gelling and melting on cooling*, *Soft Matter* 14 (31) (2018) 6431–6438, <http://dx.doi.org/10.1039/c8sm00751a>.
- [30] T.H. Niepa, L. Vaccari, R.L. Leheny, M. Goulian, D. Lee, K.J. Stebe, Films of bacteria at interfaces (FBI): Remodeling of fluid interfaces by *Pseudomonas aeruginosa*, *Sci. Rep.* 7 (1) (2017) 1–11, <http://dx.doi.org/10.1038/s41598-017-17721-3>, [arXiv:1707.04337](https://arxiv.org/abs/1707.04337).
- [31] G. Fux, G.Z. Ramon, Microscale dynamics of oil droplets at a membrane surface: Deformation, reversibility, and implications for fouling, *Environ. Sci. Technol.* 51 (23) (2017) 13842–13849, <http://dx.doi.org/10.1021/acs.est.7b03391>.
- [32] N. Segev-Mark, A. Vu, N. Chen, X. Qian, S.R. Wickramasinghe, G.Z. Ramon, Colloidal deposition on polymer-brush-coated NF membranes, *Sep. Purif. Technol.* 219 (2019) 208–215, <http://dx.doi.org/10.1016/j.seppur.2019.02.045>.
- [33] E. Yachnin, G.Z. Ramon, Direct observation of macromolecular deposition on a nanofiltration membrane, *Sep. Sci. Technol. (Philadelphia)* 52 (2) (2017) 258–265, <http://dx.doi.org/10.1080/01496395.2016.1223132>.
- [34] W.J.C. van de Ven, K.v. Sant, I.G.M. Pünt, A. Zwijnenburg, A.J.B. Kemperman, W.G.J. van der Meer, M. Wessling, Hollow fiber dead-end ultrafiltration: Influence of ionic environment on filtration of alginates, *J. Membr. Sci.* 308 (1–2) (2008) 218–229, <http://dx.doi.org/10.1016/j.memsci.2007.09.062>.
- [35] J.S. Baker, L.Y. Dudley, Biofouling in membrane systems - a review, *Desalination* 118 (1–3) (1998) 81–89, [http://dx.doi.org/10.1016/S0011-9164\(98\)00091-5](http://dx.doi.org/10.1016/S0011-9164(98)00091-5).
- [36] M. Herzberg, S. Kang, M. Elimelech, Role of extracellular polymeric substances (EPS) in biofouling of reverse osmosis membranes, *Environ. Sci. Technol.* 43 (12) (2009) 4393–4398, <http://dx.doi.org/10.1021/es900087j>.
- [37] A.W. Cense, E.A. Peeters, B. Gottenbos, F.P. Baaijens, A.M. Nuijs, M.E. van Dongen, Mechanical properties and failure of *Streptococcus mutans* biofilms, studied using a microindentation device, *J. Microbiol. Methods* 67 (3) (2006) 463–472, <http://dx.doi.org/10.1016/j.mimet.2006.04.023>.
- [38] J.K. Jiang, Y. Mu, H.Q. Yu, Differences in the colloid properties of sodium alginate and polysaccharides in extracellular polymeric substances with regard to membrane fouling, *J. Colloid Interface Sci.* 535 (2019) 318–324, <http://dx.doi.org/10.1016/j.jcis.2018.10.002>.
- [39] A. Haug, B. Larsen, O. Smidsrød, J. Møller, J. Brunvoll, E. Bunnberg, C. Djerassi, R. Records, A study of the constitution of alginic acid by partial acid hydrolysis, *Acta Chem. Scand.* 20 (1966) 183–190, <http://dx.doi.org/10.3891/acta.chem.scand.20-0183>.
- [40] G.T. Grant, E.R. Morris, D.A. Rees, P.J.C. Smith, D. Thom, Biological interactions between polysaccharides and divalent cations: The egg-box model, *FEBS Lett.* 32 (1) (1973) 195–198, [http://dx.doi.org/10.1016/0014-5793\(73\)80770-7](http://dx.doi.org/10.1016/0014-5793(73)80770-7).
- [41] B. Rehm, *Alginates: Biology and Applications*, in: *Microbiology Monographs*, vol. 13, Springer Berlin Heidelberg, Berlin, Heidelberg, 2009, <http://dx.doi.org/10.1007/978-3-540-92679-5>, [arXiv:1011.1669](https://arxiv.org/abs/1011.1669).
- [42] J. Wu, L.L. Dai, Apparent microrheology of oil - Water interfaces by single-particle tracking, *Langmuir* 23 (8) (2007) 4324–4331, <http://dx.doi.org/10.1021/la0625190>.
- [43] J. Crocker, D. Grier, Methods of digital video microscopy for colloidal studies, *J. Colloid Interface Sci.* 179 (1) (1996) 298–310, <http://dx.doi.org/10.1006/jcis.1996.0217>, [arXiv:96](https://arxiv.org/abs/96).
- [44] A. Einstein, Über die von der molekularkinetischen theorie der Wärme geforderte bewegung von in ruhenden Flüssigkeiten suspendierten teilchen, *Ann. Phys.* 322 (8) (1905) 549–560, <http://dx.doi.org/10.1002/andp.19053220806>.
- [45] T.G. Mason, K. Ganesan, J. van Zanten, D. Wirtz, S. Kuo, Particle tracking microrheology of complex fluids, *Phys. Rev. Lett.* 79 (17) (1997) 3282–3285, <http://dx.doi.org/10.1103/PhysRevLett.79.3282>.
- [46] T.G. Mason, D.A. Weitz, Optical measurements of frequency-dependent linear viscoelastic moduli of complex fluids, *Phys. Rev. Lett.* 74 (7) (1995) 1250–1253, <http://dx.doi.org/10.1103/PhysRevLett.74.1250>.

- [47] T.G. Mason, Estimating the viscoelastic moduli of complex fluids using the generalized Stokes-Einstein equation, *Rheol. Acta* 39 (4) (2000) 371–378, <http://dx.doi.org/10.1007/s003970000094>.
- [48] P. Aguilhon, M. Robitzer, L. David, F. Quignard, Structural regime identification in ionotropic alginate gels: Influence of the cation nature and alginate structure, *Biomacromolecules* 13 (1) (2012) 215–220, <http://dx.doi.org/10.1021/bm201477g>.
- [49] A. Athanassiou, D. Fragouli, I. Bayer, P. Netti, L. Rizzello, P.P. Pompa, Soft matter composites interfacing with biomolecules, cells, and tissues, in: R. Cingolani (Ed.), *Bioinspired Approaches for Human-Centric Technologies*, Springer International Publishing, 2014, pp. 29–76, http://dx.doi.org/10.1007/978-3-319-04924-3_2.
- [50] G.Z. Ramon, E.M.V. Hoek, On the enhanced drag force induced by permeation through a filtration membrane, *J. Membr. Sci.* 392–393 (2012) 1–8, <http://dx.doi.org/10.1016/j.memsci.2011.10.056>.
- [51] G.Z. Ramon, H.E. Huppert, J.R. Lister, H.A. Stone, On the hydrodynamic interaction between a particle and a permeable surface, *Phys. Fluids* 25 (7) (2013) <http://dx.doi.org/10.1063/1.4812832>.
- [52] M. Galvagno, G.Z. Ramon, Hydrodynamic-colloidal interactions of an oil droplet and a membrane surface, *Langmuir* 36 (11) (2020) 2858–2864, <http://dx.doi.org/10.1021/acs.langmuir.9b03778>.
- [53] A. Martinsen, G. Skjåk-Braek, O. Smidsrød, Alginate as immobilization material: I. Correlation between chemical and physical properties of alginate gel beads, *Biotechnol. Bioeng.* 33 (1) (1989) 79–89, <http://dx.doi.org/10.1002/bit.260330111>.
- [54] K.I. Draget, K. Steinsvåg, E. Onsjøyen, O. Smidsrød, Na- and K-alginate; effect on Ca²⁺-gelation, *Carbohydr. Polymers* 35 (1–2) (1998) 1–6, [http://dx.doi.org/10.1016/S0144-8617\(97\)00237-3](http://dx.doi.org/10.1016/S0144-8617(97)00237-3).
- [55] M.A. LeRoux, F. Guilak, L.A. Setton, Compressive and shear properties of alginate gel: Effects of sodium ions and alginate concentration, *J. Biomed. Mater. Res.* 47 (1) (1999) 46–53, [http://dx.doi.org/10.1002/\(SICI\)1097-4636\(199910\)47:1<46::AID-JBM6>3.0.CO;2-N](http://dx.doi.org/10.1002/(SICI)1097-4636(199910)47:1<46::AID-JBM6>3.0.CO;2-N).
- [56] I. Fernández Farrés, I.T. Norton, Formation kinetics and rheology of alginate fluid gels produced by in-situ calcium release, *Food Hydrocolloids* 40 (2014) 76–84, <http://dx.doi.org/10.1016/j.foodhyd.2014.02.005>.
- [57] J. Ma, Y. Lin, X. Chen, B. Zhao, J. Zhang, Flow behavior, thixotropy and dynamical viscoelasticity of sodium alginate aqueous solutions, *Food Hydrocolloids* 38 (2014) 119–128, <http://dx.doi.org/10.1016/j.foodhyd.2013.11.016>.
- [58] M. Mancini, M. Moresi, R. Rancini, Mechanical properties of alginate gels: empirical characterisation, *J. Food Eng.* 39 (4) (1999) 369–378, [http://dx.doi.org/10.1016/S0260-8774\(99\)00022-9](http://dx.doi.org/10.1016/S0260-8774(99)00022-9).
- [59] R.E. Webber, K.R. Shull, Strain dependence of the viscoelastic properties of alginate hydrogels, *Macromolecules* 37 (16) (2004) 6153–6160, <http://dx.doi.org/10.1021/ma049274n>.
- [60] J. Zhang, C.R. Daubert, E. Allen Foegeding, A proposed strain-hardening mechanism for alginate gels, *J. Food Eng.* 80 (1) (2007) 157–165, <http://dx.doi.org/10.1016/j.jfoodeng.2006.04.057>.
- [61] C.S. Lapidou, L.A. Spyrou, N. Aravas, B.E. Rittmann, Material modeling of biofilm mechanical properties, *Math. Biosci.* 251 (1) (2014) 11–15, <http://dx.doi.org/10.1016/j.mbs.2014.02.007>.
- [62] M.C. Martí-Calatayud, M. Wessling, Hydraulic impedance spectroscopy tracks colloidal matter accumulation during ultrafiltration, *J. Membr. Sci.* 535 (2017) 294–300, <http://dx.doi.org/10.1016/j.memsci.2017.04.027>.